ORIGINAL ARTICLE

lajss.org
Latin American Journal of Solids and Structures

www.lajss.org

Analytical and computational investigation of the flexural behavior of UHPFRC beams

Paulo Sergio Mota dos Santos Junior[a], Felipe Matias do Nascimento Cardoso[a], Paulo Victor Prazeres Sacramento[b], Vitor Hugo Lopes Branco[b*], Marcelo de Souza Picanço[a], Denio Ramam Carvalho de Oliveira[a]

[a] Postgraduate Program in Civil Engineering, Institute of Technology, Federal University of Para - UFPA. Belem, PA, Brazil. E-mail: paulosergiomotta2@hotmail.com; felipeufmadebalsass@gmail.com; marcelosp@ufpa.br; denio@ufpa.br
[b] Graduate Program in Materials Engineering, Federal Institute of Education, Science and Technology of Para – IFPA. Belem, PA, Brazil. E-mail: paulo.sacramento@ifpa.edu.br; vitor.branco@ifpa.edu.br

* Corresponding author

https://doi.org/10.1590/1679-78257804

Abstract

Analytical and computational calibrations and subsequent parametric analyses were performed on the four UHPFRC beams under flexure to estimate their actual shear strength. The computational models were calibrated using different values for the CDP parameters, and a finite element mesh sensitivity study was conducted. These models predicted the experimental behavior satisfactorily, and the analytical model was also able to find the beams' failure loads and proved to be a simple tool to estimate their behavior. The parametric analysis showed that the current beams did not require stirrups once the UHPFRC had high shear strength, and the maximum shear capacity was accurately determined.

Keywords

Beams, UHPFRC, Bending, NLFEA

Graphical Abstract

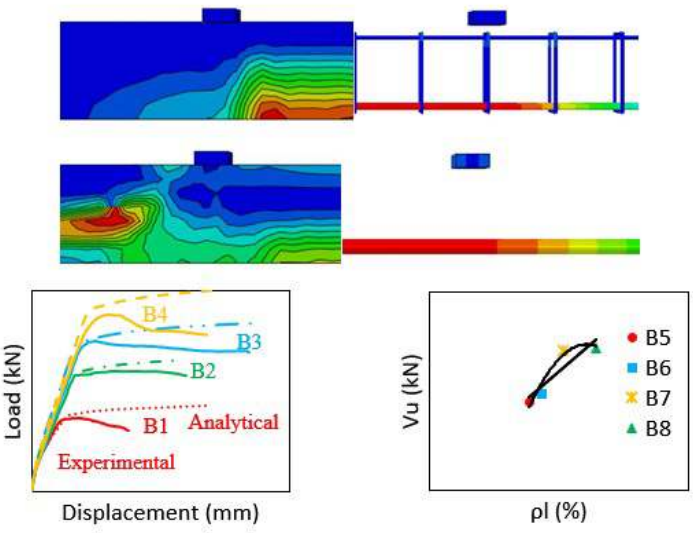

Received: August 20, 2023. In revised form: November 08, 2023. Accepted: November 22, 2023. Available online: November 28, 2023.
https://doi.org/10.1590/1679-78257804

Latin American Journal of Solids and Structures. ISSN 1679-7825. Copyright © 2023. This is an Open Access article distributed under the terms of the Creative Commons Attribution License, which permits unrestricted use, distribution, and reproduction in any medium, provided the original work is properly cited.

1 INTRODUCTION

Ultra High Performance Fiber Reinforced Concrete (UHPFRC) was developed in the mid-1990s by Richard and Cheyrezy (1995). Because of its excellent mechanical performance, it has attracted the attention of researchers and engineers for practical applications in architectural and civil structures. One of the advantages of using this composite is that, according to Farhat et al. (2007), Graybeal and Tanesi (2007), and Yoo et al. (2014) have high compressive and tensile strengths of approximately 150 and 10 MPa, respectively. As a result, structures can have a lighter weight, which makes them look slenderer. In addition, lighter loads can be applied to foundations. Other remarkable properties include excellent durability, energy absorption capacity, and fatigue performance.

Although the great potential of UHPFRC for structural applications has been demonstrated through experimental research, few studies on finite element modeling (FEM) have been carried out to predict the flexural behavior of UHPFRC beams and to provide further insights into the interaction of this ductile material with reinforcements and damage mechanisms. According to Yin et al. (2019), a reliable computational model allows an effective improvement of structural performance and reduces not only costs but also the number of laboratory tests required.

In this sense, resorting to computational analysis tools is currently a relevant practice in civil engineering because the Finite Element Modeling (FEM) method is capable of predicting both beam failure modes and crack development under loading conditions. However, nonlinear models are inherently complex because of several factors, such as the constitutive models that are used to represent materials and the problem of mesh dependency, which commonly occurs in materials that exhibit softening behavior. These variables must be understood and adapted for UHPFRC.

Some finite element (FE) software packages, namely, Abaqus, Diana, and Atena, are available with constitutive models for conventional concrete. The Concrete Damaged Plasticity (CDP) model implemented in ABAQUS is often used to predict conventional concrete behavior. However, the properties of UHPFRC are significantly different from those of conventional concrete; consequently, the parameters for CDP that establish the failure criterion, such as dilation angle (ψ), eccentricity (ϵ), fb0/fc0 (ratio of the biaxial and uniaxial compressive strengths), shape factor (k_c) and viscosity (μ), may differ from commonly used parameters. Krahl et al. (2018) developed an experimental study to determine the parameters of the CDP for UHPFRC. These parameters were computationally tested in prisms using a four-point bending test, and good results were obtained in comparison with the experimental results.

Slobbe et al. (2012) conducted a sensitivity analysis of mesh dependency and reported that the spatial discretization or topology of the finite element model can affect the numerical solution. According to the authors, mesh dependency can be subdivided into the sensitivity of crack propagation along continuous mesh lines (sensitivity to mesh polarization or mesh alignment) and the dependency of crack bandwidth on element size and orientation (sensitivity to mesh size).

Thus, further research is needed on the actual effects of not only the parameters for CDP but also of the mesh typology used in the computational models of UHPFRC beams, as there are no studies in the literature analyzing mesh sensitivity, finite element types, finite element approximation, or parameters of constitutive models. Table 1 shows the failure criteria for the CDP (implemented in the Abaqus software) used for UHPFRC in different studies. The major differences lie in the dilation angle and in the ratio of biaxial to uniaxial compressive strength f_{bc}/f_c in viscosity. The dilation angle governs the ratio of volumetric to diverting plastic strain (Abaqus, 2014), and is specific for each material. Chi et al. (2017) found a decreasing trend between the dilation angle and the properties of steel fibers. The f_{bc}/f_c ratio decreased with increasing compressive strength, as experimentally demonstrated by Speck (2008). The ratio of 1.16 was established on the basis of the findings of Kupfer et al. (1969), who reported values for the compressive strength of concrete of 18, 25, and 57 MPa. The viscosity parameter, on the other hand, is a mathematical resource to reduce the effect of permanent strain localization, which usually poses processing challenges to constitutive models that represent softening.

Therefore, a sensitivity analysis is required to apply the models to new materials. In this regard, a computational study was conducted based on experimental tests of four UHPFRC beams with different rates of flexural reinforcement, designed by Chen et al. (2018). Computational models were used to test the influence of CDP parameters, sizes and types of mesh elements, and mesh refinement. An analytical methodology was developed to determine the behavior of UHPFRC beams based on the model introduced by Fehling et al. (2014). Researchers, such as Al-Osta et al. (2017), Chen et al. (2018), Shafieifar et al. (2018), and Dogu and Menkulasi (2020), used analytical expressions to estimate the ultimate moment of UHPFRC beams. This paper presents a simplified methodology for calculating the moment-curvature and load-displacement diagrams based on the work of Yoo and Yoon (2015), which allows a more complete analysis of the behavior of beams under bending.

Table 1 Parameters for UHPFRC

Authors	CDP parameters					Mesh type	
	ψ	ϵ	f_{b0}/f_{c0}	k_c	μ	Reinforcement	Concrete
Chen and Graybeal (2012)	15º	0.1	1.16	0,667	0	C3D8R	C3D8R
Mahmud, Yang and Hassan (2013)	33º	0.1	1.16	0,660	0	-	CPS4R
Al-Osta et al. (2017)	36º	0.1	1.16	0.667	0	T3D2	C3D8(R)
Singh et al. (2017)	30º	0.1	1.05	0.667	0.005	T3D2	C3D8R
Hussein and Amleh (2018)	39º	0.1	1.16	0.667	0	T3D3	C3D8R
Krahl et al. (2018)	55º	0.1	1.07	0.667	0.0001	-	C3D8R
Shafieifar et al. (2018)	56º	0.1	1.10	0.660	0	T3D2	C3D20R
Nasrin and Ibrahim (2018)	15º	0.1	1.16	0.667	0	T3D2	C3D8(R) or C3D20(R)
Bahij et al. (2018)	36º	0.1	1.16	0.667	0	T3D2	C3D8R
Farzad et al. (2019)	39º,40º,41º	0.1	1.16	0.666	0	-	C3D8R
Kruszewski et al. (2019)	17º	0.1	1.16	0.667	0	-	C3D8R
Dogu and Menkulasi (2020)	45º	0.1	1.77	0.670	0	T3D2	C3D8R

Ψ (Dilation angle), ϵ (eccentricity), fb0/fc0 (ratio of the biaxial and uniaxial compressive strengths), kc (Shape parameter) and μ (viscosity)

2 EXPERIMENTAL MODEL

This study used four UHPFRC beams, namely B1, B2, B3, and B4, which were previously tested by Chen et al. (2018). Figures 1 and Figure 2 and Table 2 show the geometric properties of the beams, as well as details of the reinforcements. Tables 3 and Table 4 show the mechanical properties of steel and concrete, respectively.

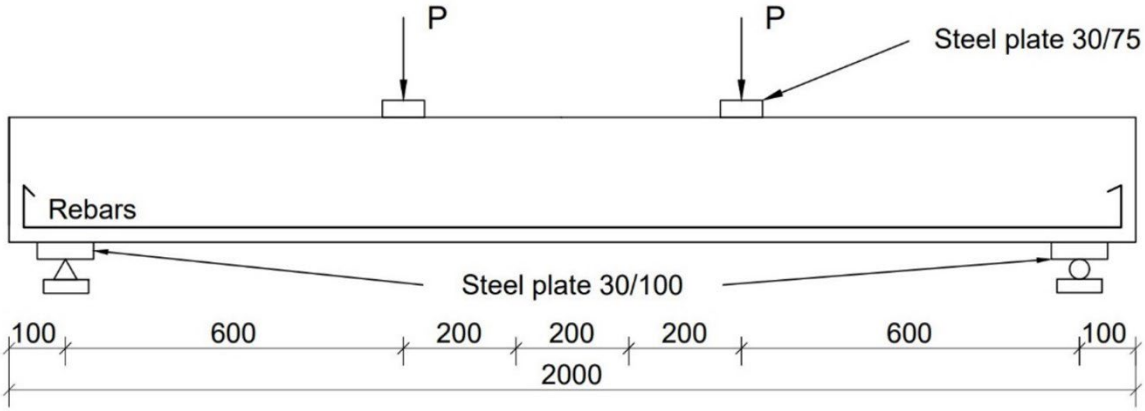

Figure 1 Beam geometry, reinforcement and loading

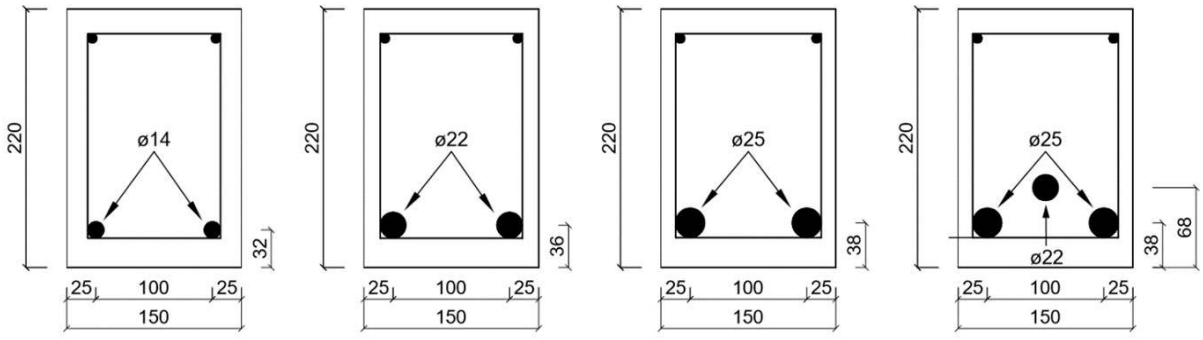

Figure 2 Cross section of the beams

Table 2 Beam details - Chen et al. (2018)

Beam	a	d	a/d	ρ_l	ρ_w	V_f (%)	Stirrups
B1	600	188.0	3.19	1.09	0.45	2	8 mm @150
B2		184.0	3.26	2.75	0.45	2	8 mm @150
B3		182.0	3.29	3.60	0.67	2	8 mm @100
B4		173.6	3.45	5.23	1.12	2	8 mm @60

Table 3 Concrete properties - Chen et al (2018)

Elastic Modulus ($E_ç$)	Poisson's ratio (v)	Compressive strength ($f_ç$)	Tensile strength (f_{tcm})
GPa	-	MPa	MPa
41.64	0.2	141.50	8.15

Table 4 Steel properties - Chen et al. (2018)

Reinforcement	Diameter (Ø)	Yield stress (σ_{ys})	Yield strain (ε_{ys})	Elastic Modulus (E_s)	Poisson's ratio (v)
-	mm	MPa	‰	GPa	-
D14	14	461	2.30	200	0.3
D22	22	417	2.08		
D25	25	456	2.28		

3 COMPUTATIONAL MODEL

Figure 3 shows the computational model designed according to the specifications for the geometry, loadings, and boundary conditions presented above. An embedded region constraint was assigned to the interaction between the reinforcement and concrete, simulating perfect adhesion between the steel and concrete. The interaction between the steel plates and the beam was modeled using a tie constraint. Thus, the possibility of displacement at the interface was disregarded. The steel plates were assumed to exhibit linear elastic behavior. The reference points (RPs) created to apply the loads and constraints on the supports were linked to the surfaces of the plates using coupling constraints.

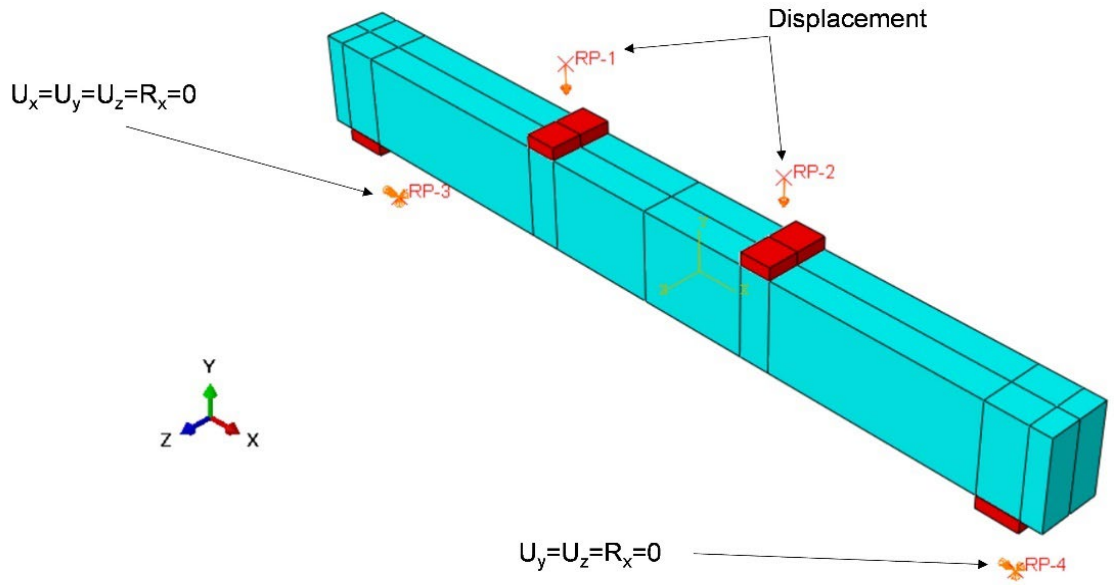

Figure 3 Geometry, loads and boundary conditions

The CDP model was used to characterize the mechanical behavior of UHPFRC, implemented in the Abaqus software package (Abaqus, 2014). This model enables the representation of the nonlinear behavior of concrete under uniaxial, biaxial, and triaxial stresses. In addition, the model can record the degradation of stiffness (damage) and permanent

strains (plasticity) that are typical of concrete. The plastic damage model was based on the model proposed by Lubliner et al. (1989) and Lee and Fenves (1998). According to Kmiecik and Kamiński (2011), this model is an adaptation of the Drucker-Prager model, which is also used to demonstrate the behavior of brittle materials. According to Abaqus (2014), this model is intended for the analysis of reinforced concrete structures under monotonic, cyclic, random or dynamic loadings.

Figure 4 shows the stress-strain curve calibrated by Krahl et al. (2018) that was used to represent the compression behavior of UHPFRC, with a fiber volume of 2%, according to the mechanical characteristics of concrete reported in Table 3. The authors used the model of Carreira and Chu (1985) to represent the stress-strain behavior of UHPFRC under compression loading. For the post-peak interval, two constants (k_1 and k_2), proposed by Mansur et al. (1999), were added to the equation to simulate the effect of fiber addition, according to Equations 3 and 4, where the constants were only considered in the post-peak branch. σ_0, ε_0, E_{c0} are peak stress, peak strain and initial elastic modulus, respectively, and they are known parameters. k_1 and k_2 are parameters based on experiments with the post-peak branch of the experimental results. Mansur et al. (1999) proposed equations for these variables that depend on fiber volume and peak stress of concrete (σ_0). In the study developed by Krahl et al. (2018), k_1 and k_2 were calibrated for parameter β, and total energy (W_c) corresponds to the average area of the experimental stress-strain curves of concrete. For the present study, k_1 k_2, β and W_c are 0.15, 0.30, 6.5 and 1.11 MPa, respectively.

$$\sigma = \sigma_0 \left[\frac{k_1 \beta \frac{\varepsilon}{\varepsilon_0}}{k_1 \beta - 1 \left(\frac{\varepsilon}{\varepsilon_0}\right)^{k_2 \beta}} \right] \tag{1}$$

$$\beta = \frac{1}{1 - \frac{\sigma_0}{\varepsilon_0 E_{c0}}} \tag{2}$$

$$k_1 = 0.42539 - 0.04942\beta - 0.2071 W_c + 0.00186\beta^2 + 0.16163 W_c^2 \tag{3}$$

$$k_2 = 1.19603 - 0.09059\beta - 0.82313 W_c + 0.00329\beta^2 + 0.37862 W_c^2 \tag{4}$$

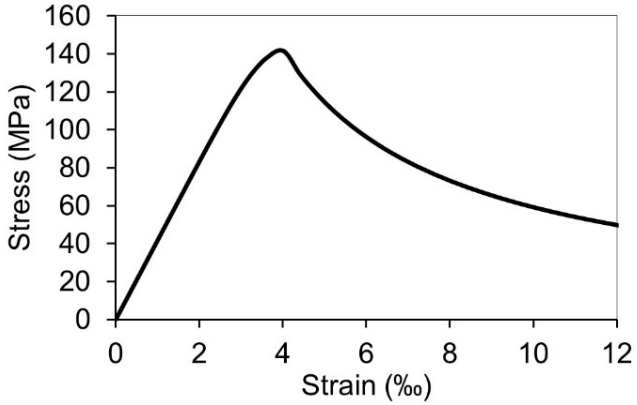

Figure 4 Behavior of concrete under uniaxial compression

The tensile behavior of UHPFRC was determined using the constitutive law for stress-energy fracture. Fracture energy (G_f) is calculated by Equation 5, according to Wille et al. (2014), where V_f is fiber volume ratio. Considering that the models used UHPFRC with 2% fiber volume, fracture energy was calculated to be $20{,}4\ kN/m$. Tensile strength of UHPFRC was calculated with Equation 6, proposed by Schmidt (2008), where f_{ctm} is the average tensile strength of UHPFRC and f_{ck} is its characteristic compressive strength.

$$G_f = -1.4 \cdot {V_f}^2 + 13 \cdot V_f \tag{5}$$

$$f_{ctm} = 0{,}3 \cdot (f_{ck})^{2/3} \tag{6}$$

Simulations of the reinforcements were performed by considering the perfect constitutive elastoplastic model associated with the Von Mises yield criterion. Table 4 lists the elastic modulus and yield stress of each rebar. Poisson's ratio was assumed to be 0.3. The material underwent plastic strain, as shown in Table 4.

4 MOMENT-CURVATURE DIAGRAM

For an analytical estimation of the experimental behavior of the beams, the moment-curvature diagrams were first determined for each beam, followed by the calculation of the load-displacement curves.

The moment-curvature diagrams were calculated using the equilibrium equations of the UHPFRC cross-sections designed by Leutbecher and Fehling (2013) and Fehling et al. (2014). Figure 5 shows the distribution of stresses and strains for a rectangular cross-section under axial force (N) and bending moment (M).

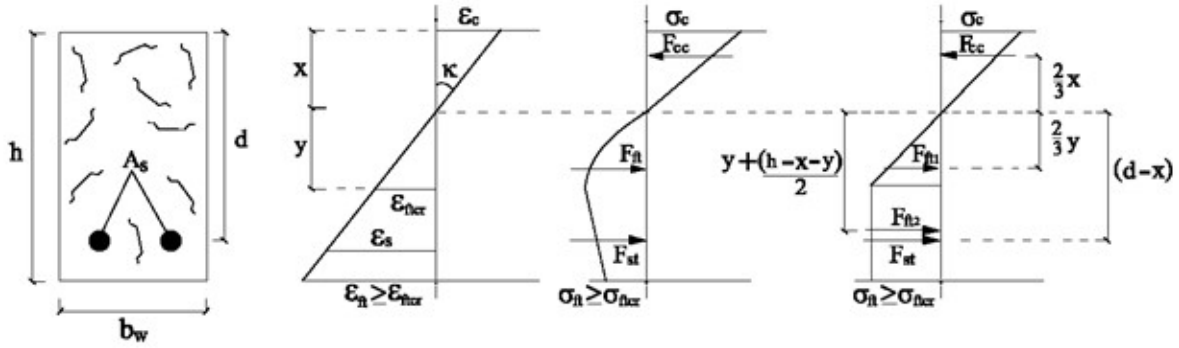

Figure 5 Stress and strain diagrams for cracked cross section

It should be noted that x is the position of the neutral axis; F_{cc} is the force resulting from compression of UHPFRC, acting at $x/3$; F_{ft1} and F_{ft2} are the forces resulting from tensile stress on UHPFRC, acting $y/3$ and $y + (h - x - y)/2$, respectively; F_{st} is the force resulting from the reinforcements.

The distribution of the tensile stresses on the concrete beams was simplified. There was triangular behavior for the linear-elastic branch and rectangular behavior for the branch where cracking occurred. This distribution is given by Equations 7 and 8, respectively, where h stands for beam height; x is the depth of the neutral axis; b is beam thickness; σ_{ftcr} is the cracking stress of UHPFRC; y it is height that limits the branch between cracked and non-cracked concrete, as given by Equation 9.

$$F_{ft1} = \begin{cases} 0{,}5 \cdot (h - x) \cdot b \cdot E_c \cdot \varepsilon_{ft} \; \varepsilon_{ft} < \varepsilon_{ftcr} \\ 0{,}5 \cdot y \cdot b \cdot \sigma_{ftcr} \; \varepsilon_{ft} \geq \varepsilon_{ftcr} \end{cases} \tag{7}$$

$$F_{ft2} = \{(h - x - y) \cdot b \cdot \sigma_{ftcr} \; \varepsilon_{ft} \geq \varepsilon_{ftcr} \tag{8}$$

$$y = \left\{ \frac{\varepsilon_{ftcr}}{\varepsilon_{ft}} \cdot (h - x) \; \varepsilon_{ft} \geq \varepsilon_{ftcr} \right. \tag{9}$$

Distribution of the resultant compressive force (F_{cc}) is determined according to Equation 10. Tensile strength in steel (F_{st}) is given by Equation 11, where calculation of stress in the reinforcements is based on the perfect elastoplastic constitutive mode. Equations 7, 8, 10, and 11 were used to establish the balance of forces, according to Equation 12. In relation to the neutral axis (x), the bending moment was calculated as shown in Figure 6 and Equation 13. One compressive strain value was assumed for concrete (ε_c), and the neutral axis (x) was made to range from 0 to h, until the forces were balanced (Equation 12). Subsequently, curvature (k), strain in the reinforcements (ε_{st}) and tensile strain of concrete (ε_{ft}) were calculated according to Equations 14, 15 and 16, respectively. Importantly, equations 14,15 and 16 represent the compatibility of the strains in the cross-section, as shown in Figure 5. According to Yoo and Yoon (2015), the moment-curvature curve can be converted to a load-displacement curve using Equations 17 and 18.

$$F_{cc} = \begin{cases} 0{,}5 \cdot x \cdot b \cdot E_c \cdot \varepsilon_{ft} \; \varepsilon_{ft} < \varepsilon_{ftcr} \\ 0{,}5 \cdot x \cdot b \cdot E_c \cdot \varepsilon_c \; \varepsilon_{ft} \geq \varepsilon_{ftcr} \end{cases} \tag{10}$$

$$F_{st} = \begin{cases} \varepsilon_{ft} \cdot E_c \cdot A_s \; \varepsilon_{st} < \varepsilon_{ys} \\ A_s \cdot \sigma_{ys} \; \varepsilon_{st} \geq \varepsilon_{ys} \end{cases} \tag{11}$$

$$0 = -F_{cc} + F_{ft1} + F_{ft2} + F_{st} \tag{12}$$

$$M = F_{cc} \cdot \left(x - \frac{1}{3}x\right) + F_{ft1} \cdot \left(y - \frac{1}{3}y\right) + F_{ft2} \cdot \left(y + \frac{h-x-y}{2}\right) + F_{st} \cdot (d - x) \tag{13}$$

$$k = \frac{\varepsilon_c}{x} \tag{14}$$

$$\frac{\varepsilon_c}{x} = \frac{\varepsilon_{st}}{d-x} \tag{15}$$

$$\frac{\varepsilon_c}{x} = \frac{\varepsilon_{ft}}{h-x} \tag{16}$$

$$\frac{M}{k} = EI \tag{17}$$

$$\delta_{max} = \frac{Pa}{24EI}(3L^2 - 4a^2) \tag{18}$$

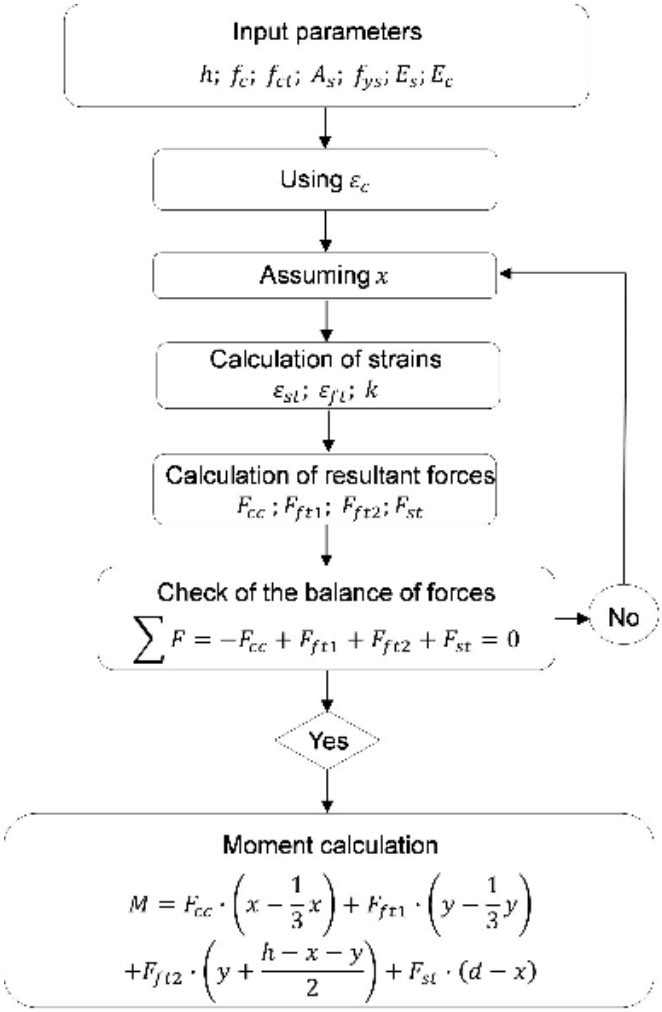

Figure 6 Flowchart to determine the moment-curvature diagram

5 CALIBRATION

A mesh sensitivity study was conducted using Beam B1. Four discretization were used for the solid and rebar elements (60 mm, 50 mm, 40 mm, and 30 mm) to assess how the mesh affected the responses of the models. This assessment was carried out to obtain a mesh that had a low computational cost and adequately represented the experimental failure mode.

Two types of solid elements were tested: a mesh with hexahedral elements and a mesh with tetrahedral elements, as shown in Figures 7 and Figure 8. In both cases, quadratic approximations were used for the displacements, referred to as C3D8 (R)/C3D20 (R) and C3D4/C3D10. Elements T3D2 and T3D3 were used in the rebar elements, for example, the longitudinal reinforcements. Table 5 lists all types of finite elements used for the modeling.

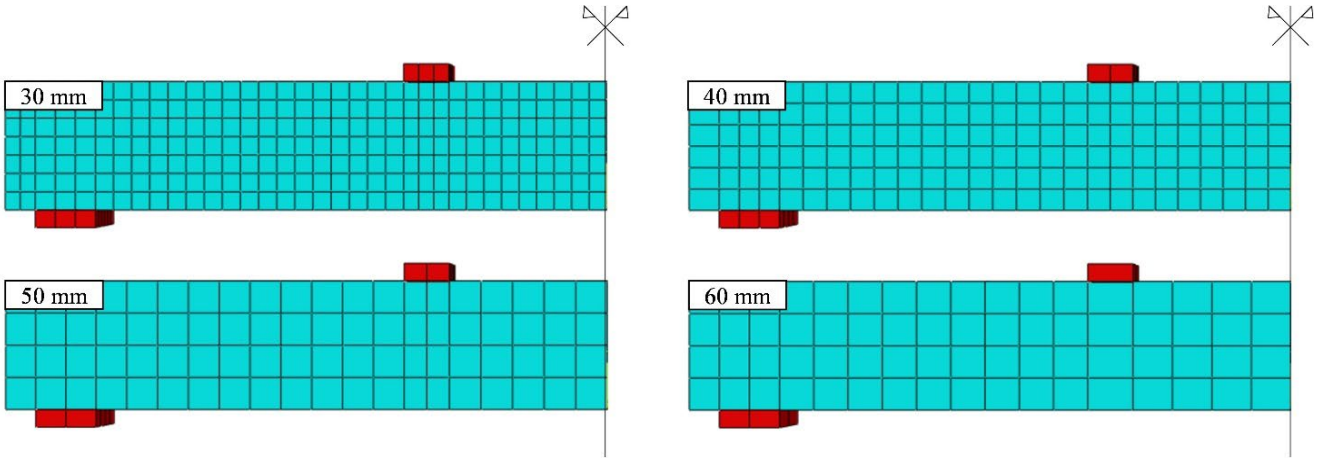

Figure 7 Variation in the size of the hexahedral mesh for the elements C3D8 (R) and C3D20 (R)

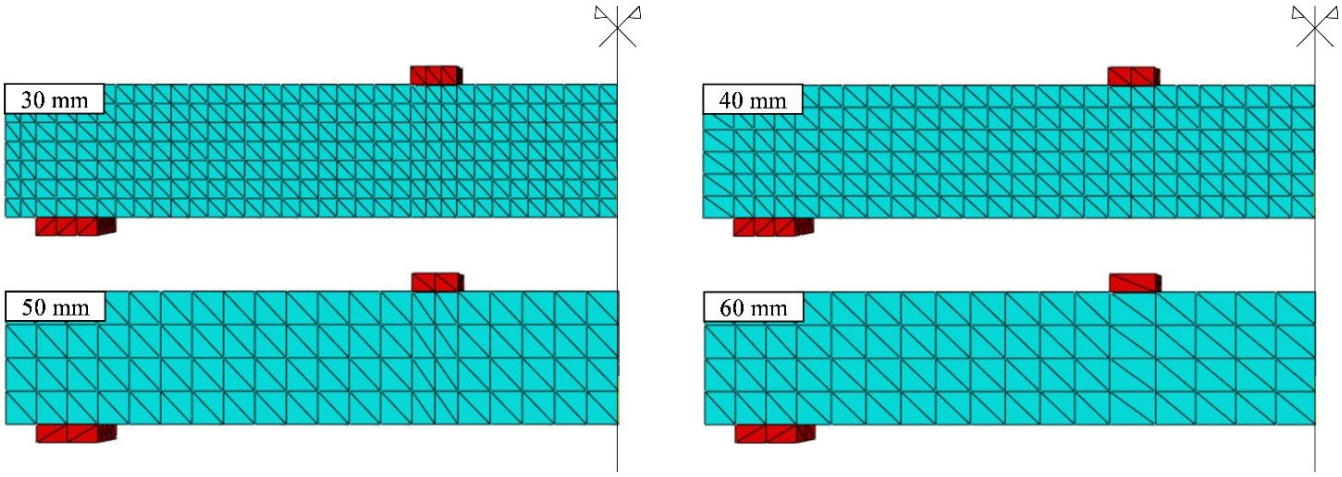

Figure 8 Variation in the size of the tetrahedral mesh for elements C3D4 and C3D10

Table 1 shows that the parameters for the CDP used as a starting point for these analyses were the same as those experimentally calibrated by Krahl et al. (2018). However, a parametric analysis was performed while varying the parameters for CDP to assess how they could affect the response of the models, since other recommendations of these parameters for UHPFRC have been reported in the literature.

All models accurately captured the beginning of cracking as well as the post-cracking regime up to the peak load. Therefore, they are suitable for predicting the behavior of beams in a linear elastic regime. However, the maximum load and post-peak branch were better characterized by the models containing hexahedral finite elements with linear approximation and reduced integration (C3D8R) and sizes of 50 mm and 60 mm, and with reinforcements that were simulated with elements T3D2/T3D3, as shown in Figures 9g and 9h. In comparison, the other models presented a high computational cost and overestimated the beam tenacity after the application of the maximum load.

Table 5 Types of finite elements

C3D8		**C3D8R**	
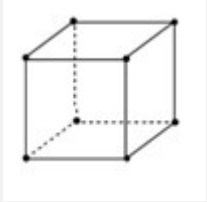	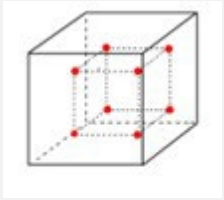	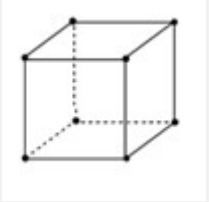	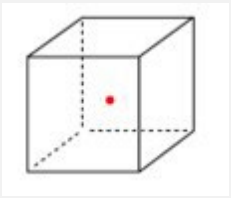
8 nodes	8 integration points	8 nodes	1 integration point
C3D20		**C3D20R**	
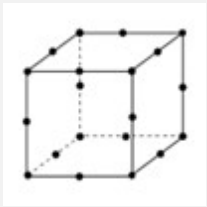	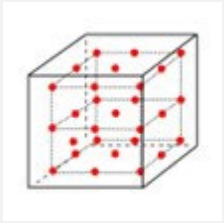	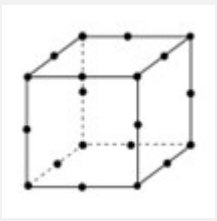	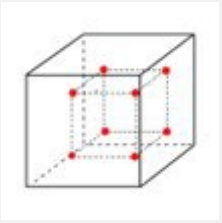
20 nodes	27 integration points	20 nodes	8 integration points
C3D4		**C3D10**	
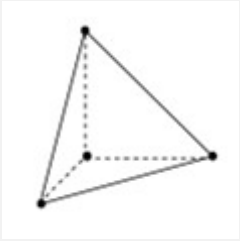	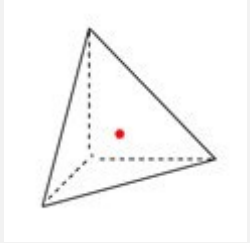	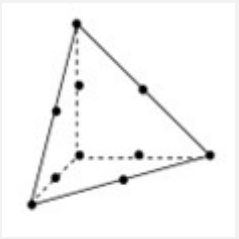	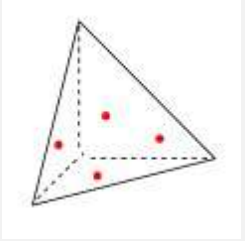
4 nodes	1 integration point	10 nodes	4 integration points
T3D2		**T3D3**	
			
2 nodes	1 integration point	3 nodes	2 integration points

Therefore, finite elements (C3D8R/T3D2) were chosen for subsequent analyses. When it comes to a model that considers the nonlinearity of materials, it is clear that the mesh size can have a significant impact on the behavior of the models. In their research, Genikomsou and Polak (2016) showed that even when using very similar mesh sizes (15 mm, 20 mm and 24 mm), the models behaved considerably different in the tests.

Slobbe et al. (2012) reported that the spatial discretization or mesh topology of the finite element model influences the numerical solution. According to the author, mesh dependence can be subdivided into the sensitivity of crack propagation along the continuous mesh lines (mesh polarization sensitivity or mesh alignment) and the dependency of crack bandwidth on the size and orientation of the element (mesh size sensitivity).

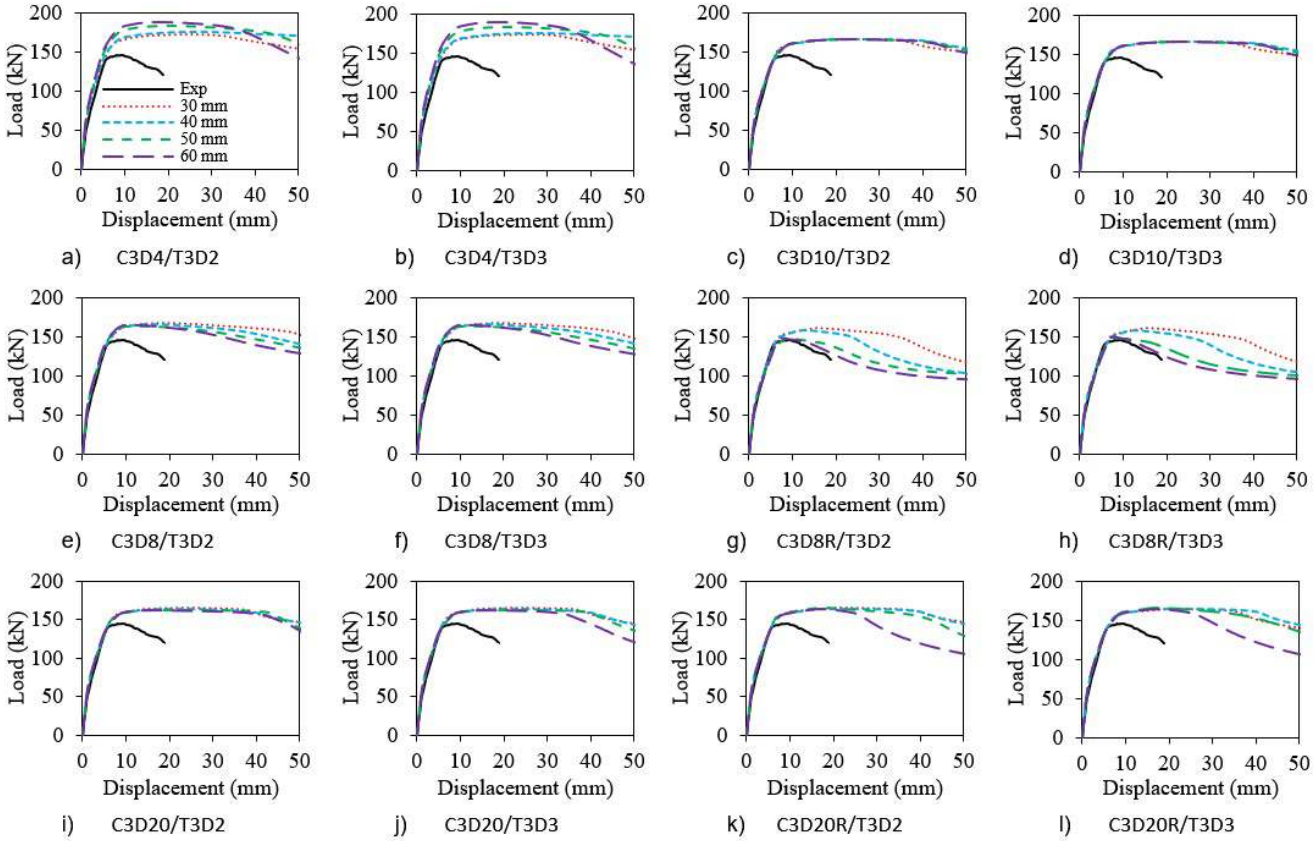

Figure 9 Mesh study

A study was conducted to assess the influence of CDP-related parameters for beam B1, such as the dilation angle (ψ), eccentricity (ϵ), biaxial-to-uniaxial strength ratio (f_{bc}/f_c), shape factor k_c, and viscosity (μ). The results are shown in Figure 10.

Figure 10 shows that the variation in the parameters for the CDP did not significantly change the behavior of the beams, with the exception of eccentricity and viscosity (see Figure 10b and 10e). This is because the UHPFRC is a highly ductile material. Brittle materials, such as conventional concrete, are greatly influenced by the variation in these parameters, especially the dilation angle, as can be seen in the study developed by Genikomsou and Polak (2015).

Eccentricity defines the approach speed of the plasticity potential function asymptote (Labibzadeh, 2020) and is used to model the nonlinear behavior and damage progression in concrete structures (Benin et al., 2020). In this study, values greater than 0.1 showed post-peak hardening behavior, which does not corroborate the expected results.

Viscosity is a parameter used to solve the numerical convergence problems. Michal and Andrzej (2015) studied this parameter and noted that values between 0 to 10^{-3} did not significantly affect the results. However, when adopting viscosity values above 10^{-3}, the computational results found by the authors were overestimated; this is because the higher this parameter is, the greater the stress redistribution along the structural element will be.

The use of small values can improve the convergence rate and processing time without compromising results. Adopting a viscosity value $\mu = 10^{-4}$ resulted in a good response when compared to the experimental one, in addition to a short processing time. Therefore, the parameters for the CDP adopted for all beams are the same as those determined by Krahl et al. (2018) (see Table 1).

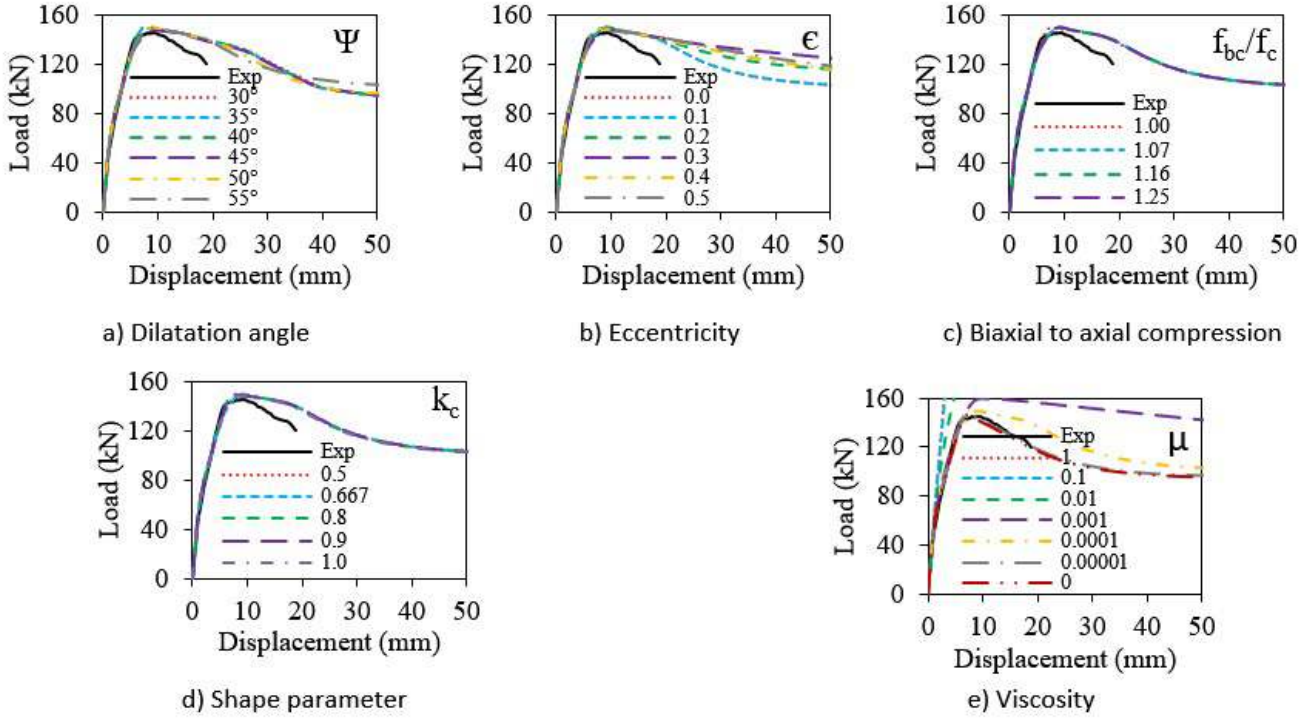

Figure 10 Assessment of parameters for CDP

6 RESULTS

Figures 11a and 11b show the moment-curvature and load-displacement diagrams of the beams, respectively. The results of the load-displacement diagram of the analytical and experimental models were very similar. Therefore, the analytical methodology satisfactorily predicted the behavior of UHPFRC beams.

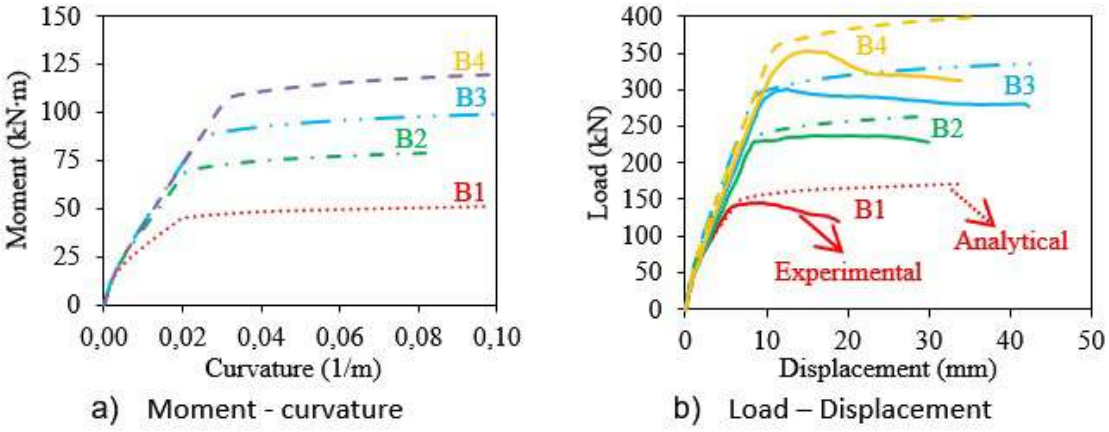

Figure 11 Diagrams for the behavior of the beams

The models were processed with the parameters for the CDP, as shown in Table 1, and with elements C3D8R and T3D2 for concrete and reinforcement, respectively. All computational models satisfactorily represented the experimental behavior of the beams. The difference in the maximum load with the mesh size variation was less than 8%, as shown in Table 6. As can be seen in Figure 12, the models B1 and B4 showed a better post-failure behavior for mesh sizes of $50\ mm$ and $60\ mm$; by contrast, models B2 and B3 outperformed in the post-peak branch with mesh sizes of $30\ mm$ and $40\ mm$.

Figure 13 shows the crack maps of the computational models for the 30 mm mesh together with the stress distribution in the reinforcement. All computational models predicted flexural failure and showed that cracking was more intense between load application points. The yield started in the longitudinal reinforcements under tensile stress immediately before the beams reached the failure load.

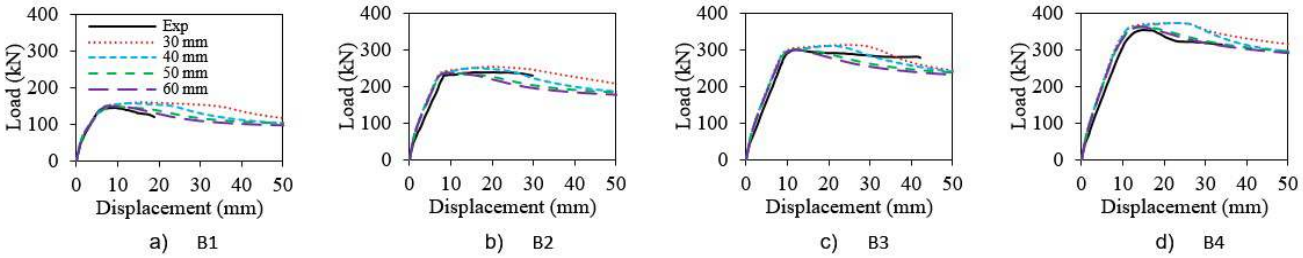

Figure 12 Load curve versus displacement of the beams

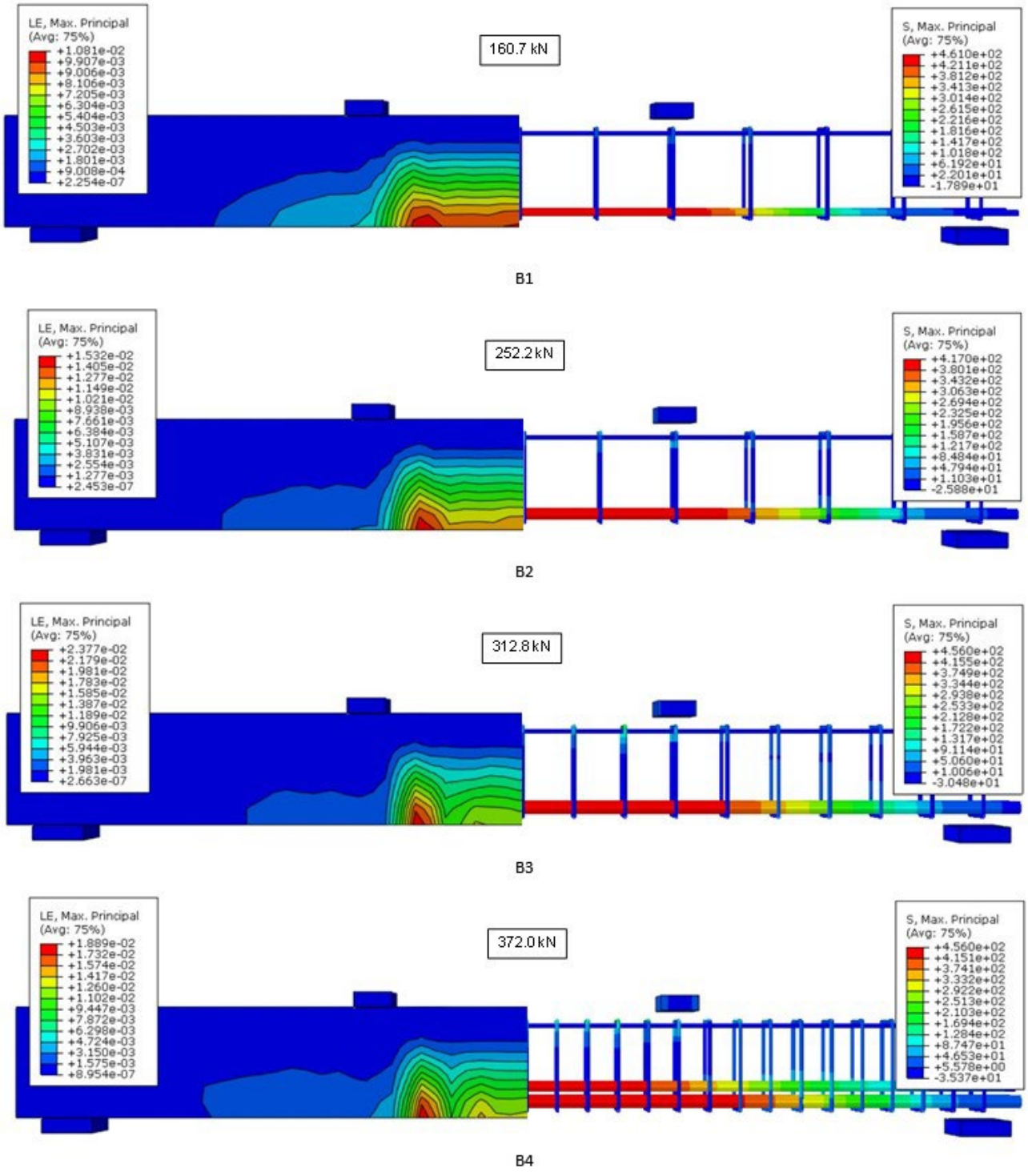

Figure 13 Maps of beam cracks and stress in the reinforcements

Table 6 Experimental and computational results at failure

Specimen	Experimental		Mesh							
			30 mm		40 mm		50 mm		60 mm	
	Load kN	Disp. mm	Load kN	Disp. mm	Load kN	Disp. mm	Load kN	Disp. mm	Load kN	Disp. mm
B1	144.2	8.91	160.7	15.20	158.0	12.78	148.0	8.34	148.0	7.14
B2	238.0	16.15	252.2	19.21	249.1	14.59	236.5	8.81	235.9	8.82
B3	301.3	12.50	312.8	24.48	310.9	21.01	299.4	11.21	298.6	11.19
B4	353.1	14.91	372.0	22.38	371.3	22.45	362.0	14.14	361.4	13.75

7 PARAMETRIC STUDY

Based on the calibration of computational models, a parametric study can be conducted to obtain more information on the final capacity of the beams. The new models evaluated the effects of the transverse (ρ_w) and longitudinal (ρ_l) reinforcement ratios on the shear strength of the beams. Overall, a parametric study was performed for 20 cases, as shown in Figure 14 and Table 7.

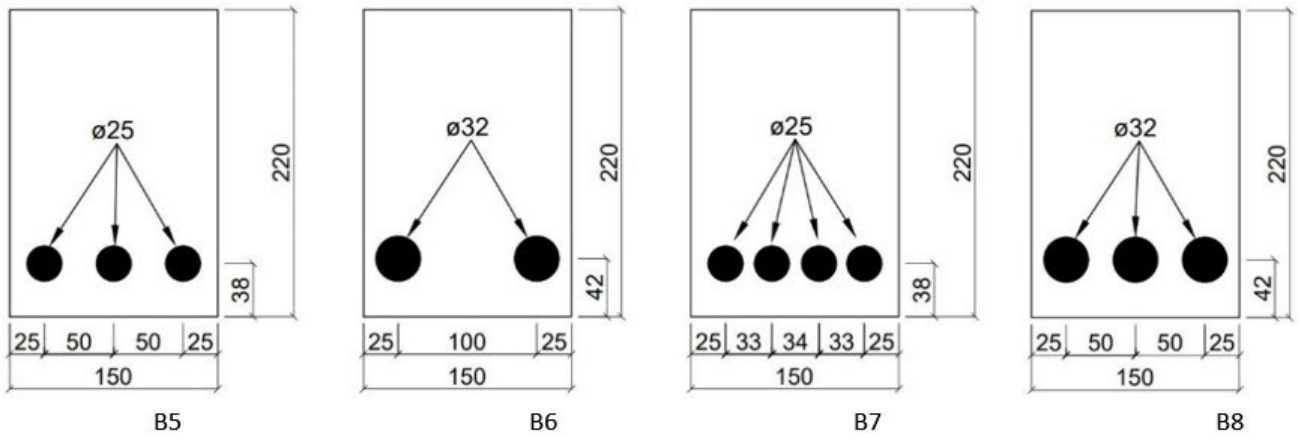

Figure 14 Cross section of the beams

Table 7 Cases considered for the numerical parametric study

Series	Variable	f_{ys} MPa	a/d	ρ_l (%)	ρ_w (%)	V_f (%)	Stirrups
B1	-	461	3.19	1.09	0.45	2	8 mm @150
B1-I	ρ_w				-		-
B2	-	417	3.26	2.75	0.45	2	8 mm @150
B2-I	ρ_w				-		-
B3	-	456	3.29	3.60	0.67	2	8 mm @100
B3-I	ρ_w				-		-
B4	-	417 and 456	3.45	5.23	1.12	2	8 mm @60
B4-I	ρ_w				-		-
B5	ρ_l	456, 500, 550 and 600	3.29	5.39	-	2	-
B6	ρ_l	456, 500, 550 and 600	3.37	6.02	-	2	-
B7	ρ_l	456, 500, 550 and 600	3.29	7.19	-	2	-
B8	ρ_l	456, 500, 550 and 600	3.37	9.03	-	2	-

Figure 15 shows the results for models B1-I, B2-1, B3-I, and B4-I. These models are similar to those of Figure 2, but the difference lies in the fact that they do not have transversal reinforcement. When comparing the load-displacement diagrams in Figure 15 (without stirrups) with those in Figure 12 (with stirrups), the difference is insignificant; that is, the transverse reinforcement ratio does not change the behavior of the beams or their failure modes. Therefore, for these UHPFRC beams, there is no need to use shear reinforcement, which would consequently reduce the cost of labor and materials.

In this regard, through experimental research, Gomaa and Alnaggar (2019) showed that for UHPFRC with 2% fiber content, the failure mode of the beams changed from shear failure to bending failure. This finding confirms the high shear strength achieved by Ultra High-Performance Concrete.

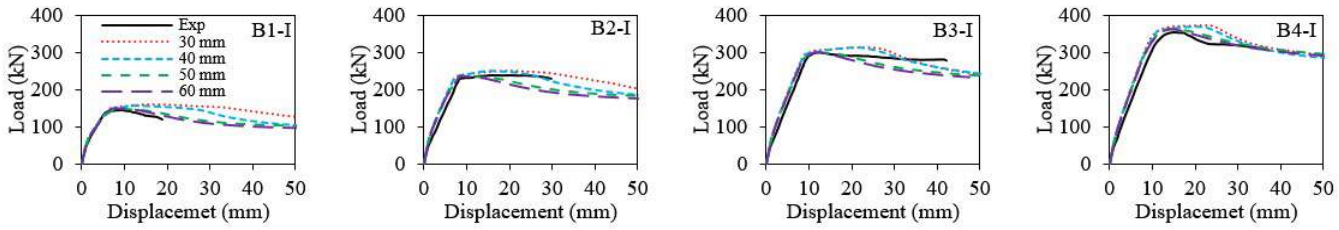

Figure 15 Load-displacement curve of the beams without stirrups

To assess the shear strength of the beams without transverse reinforcement, different values were used for the ratio and yield stress in the longitudinal reinforcements. Figures 16 - 18 show that models B7 (f_y = 600 MPa) and B8 (f_y = 500, 550 and 600 MPa) exhibited shear failure, whereas the others exhibited flexural failure, with yield stress in the longitudinal reinforcement. It should be emphasized that models B5, B6, B7, and B8 are those without transverse reinforcement.

Bahij et al. (2018) conducted experimental studies on UHPFRC beams with similar characteristics to those of the present study; they used steel rebars with high tensile strength (1320 MPa) and with flexural reinforcement ratios of approximately 2.0% and 3.0%. In the present study, the steel rebars of choice were those with yield stress ratios similar to those of the experimental models.

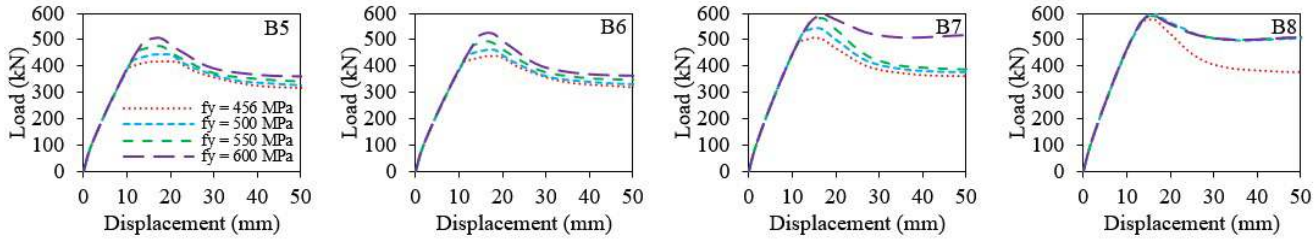

Figure 16 Load-displacement curve of the beams (30 mm mesh)

When comparing the experimental beams (B1, B2, B3, and B4) with the model having the lowest shear strength B6 (f_y = 600 MPa), it was found that these beams failed by 27.4%, 45.3%, 57.3%, and 67.2% of their shear strength capacity, respectively.

As concrete was crushed with a longitudinal reinforcement ratio of 9.03% for model B8 (f_y = 600 MPa), a parametric study of the beams with stirrups was not carried out because a higher ratio would be needed for beam shear failure to occur; however, the limiting factor would still be the crushing of concrete, as can be seen in Table 8 and Figure 17. Graphically, at the maximum load frame, as shown in Figure 18, for the output variable LE, ultimate concrete strain, and S, the ultimate reinforcement stress.

Table 8 Computational results of the parametric study of the beams

Specimen	456 MPa			500 MPa			550 MPa			600 MPa		
	Load *kN*	Disp. *mm*	Failure Mode	Load *kN*	Disp. *mm*	Failure Mode	Load *kN*	Disp. *mm*	Failure Mode	Load *kN*	Disp. *mm*	Failure Mode
B5	416.4	19.4	Flexure	446.9	18.5	Flexure	477.9	17.2	Flexure	505.8	17.5	Flexure/Shear
B6	436.0	17.6		465.2	17.1		495.3	16.9		525.2	16.9	
B7	509.4	15.3		544.8	15.9		582.4	16.8		599.8	17.1	Shear
B8	576.4	15.8		605.1	16.1		588.8	16.3	Shear	588.8	16.3	

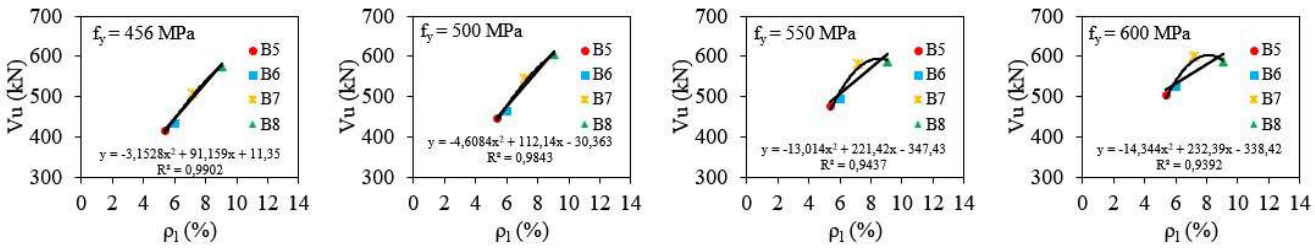

Figure 17 Ultimate load diagram versus longitudinal reinforcement ratio of the beams

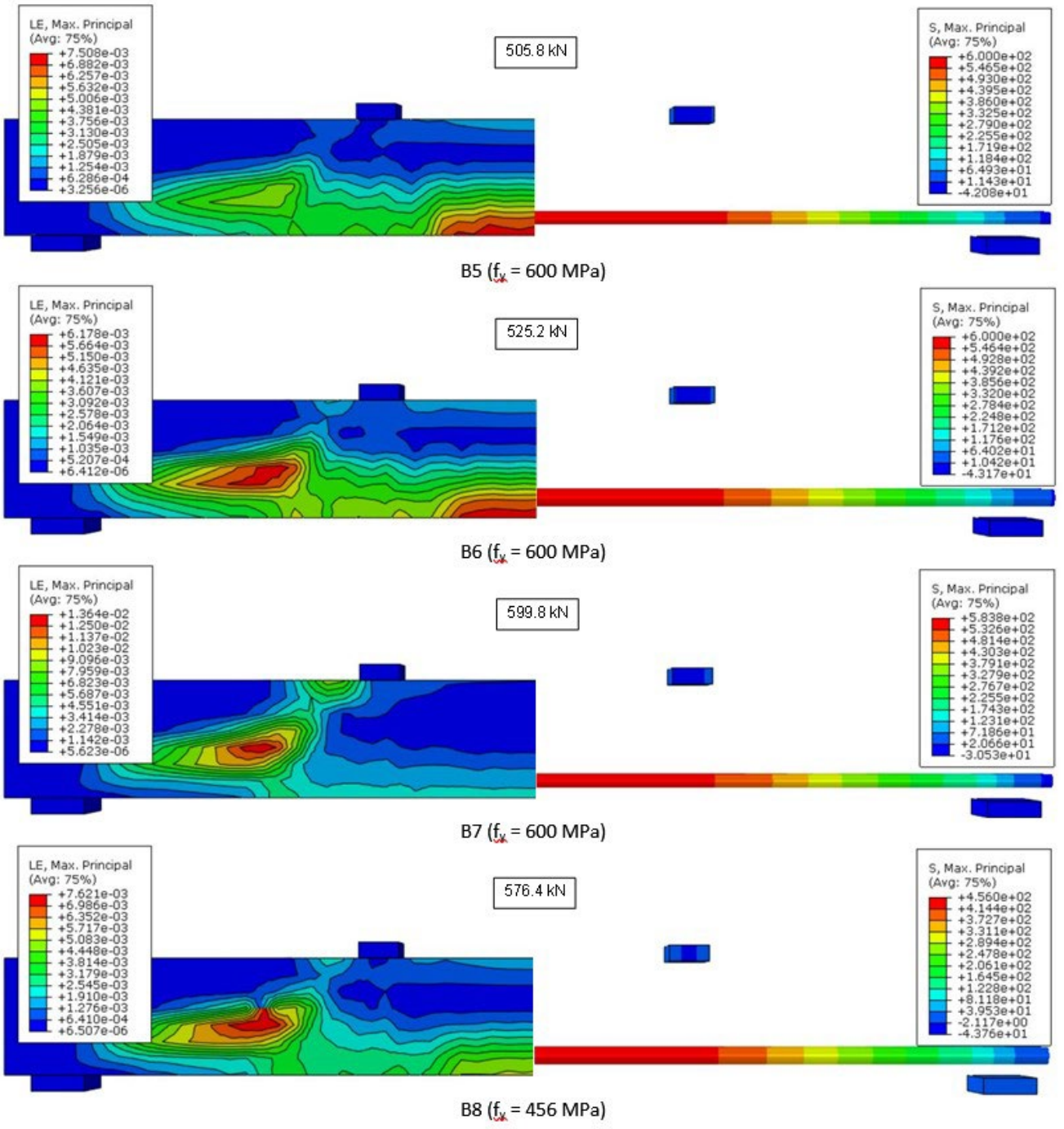

Figure 18 Map cracking of the beams and tensile stress in the reinforcements (30 mm mesh)

8 CONCLUSION

This study reported the results of the analytical and computational calibrations of four UHPFRC beams. The calibration of the computational models used different parameters for the CDP, as well as different mesh sizes and types for the finite element analysis. The calibrated models satisfactorily predicted the experimental behavior. The parametric analysis showed that the beams did not require stirrups because the UHPFRC had high shear strength. Finite elements C3D8R / T3D2 has been shown to be effective for use in UHPFRC beams. The analytical model was able to satisfactorily predict the failure load of the beams and proved to be a simple tool for estimating the behavior of UHPFRC beams.

Acknowledgements

The authors gratefully acknowledge the support from CNPQ, CAPES, UFPA and IFPA.

Author's Contribuitions: Conceptualization, Denio Ramam and Vitor Branco; Methodology, Paulo Mota, Paulo Sacramento and Vitor Branco, Investigation, Paulo Mota, Felipe Matias, Paulo Sacramento; Writing - original draft, Paulo Mota and Vitor Branco; Writing - review and editing, Denio Ramam and Marcelo Souza; Resources, Paulo Mota; Supervision, Denio Ramam.

Editor: Marco L. Bittencourt

References

Abaqus Theory Manual (6.14). (2014). Dassault Systems, Providence, RI, USA.

Benin, A., Guzijan-Dilber, M., Diachenko, L., & Семенов, A. C. (2020). Finite element simulation of a motorway bridge collapse using the concrete damage plasticity model. E3S Web of Conferences, 157, 06018. doi.org/10.1051/e3sconf/202015706018.

CARREIRA, Domingo J.; CHU, Kuang-Han. (1985). Stress-strain relationship for plain concrete in compression. In: Journal Proceedings. p. 797-804.

CHEN, Linfeng; GRAYBEAL, Benjamin A. (2012). Modeling structural performance of ultrahigh performance concrete I-girders. Journal of Bridge Engineering, v. 17, n. 5, p. 754-764.

CHI, Yin et al. (2017) Finite element modeling of steel-polypropylene hybrid fiber reinforced concrete using modified concrete damaged plasticity. Engineering Structures, v. 148, p. 23-35.

DOGU, Mehmet; MENKULASI, Fatmir. (2020). A flexural design methodology for UHPC beams posttensioned with unbonded tendons. Engineering Structures, v. 207, p. 110193.

DY Yoo, HO Shin, JM Yang, YS Yoon. (2014). Material and bond properties of ultra-high-performance fiber reinforced concrete with micro steel fibers. Composites Part B: Engineering, Elsevier, v. 58, p. 122–133.

E Fehling, M Schmidt, J Walraven, T Leutbecher, S Fröhlich. (2014). Ultra-High-Performance Concrete UHPC. Ernst and Sohn. Wiley Online Library.

FA Farhat, D Nicolaides, A Kanellopoulos (2007). High-performance Fiber-reinforced cementitious composite (CARDIRF)–performance and application to retrofitting. Engineering Fracture Mechanics, Elsevier, v. 74, n. 1-2, p. 151–167.

FARZAD, Mahsa; SHAFIEIFAR, Mohamadreza; AZIZINAMINI, Atorod. (2019). Experimental and numerical study on bond strength between conventional concrete and Ultra High-Performance Concrete (UHPC). Engineering Structures, v. 186, p. 297-305.

GENIKOMSOU, A. S., & POLAK, M. A. (2016). Finite-element analysis of reinforced concrete slabs with punching shear reinforcement. Journal of Structural Engineering, 142(12), 04016129, p. 1-16.

GENIKOMSOU, Aikaterini S.; POLAK, Maria Anna. (2015). Finite element analysis of punching shear of concrete slabs using damaged plasticity model in ABAQUS. Engineering Structures, v. 98, p. 38-48.

GOMAA, Shady; ALNAGGAR, Mohammed. (2019). Transitioning from Shear to Flexural Failure of UHPC Beams by Varying Fiber Content. In: International Interactive Symposium on Ultra-High-Performance Concrete. Iowa State University Digital Press,

GRAYBEAL, B.; TANESI, J. (2007). Durability of an ultrahigh-performance concrete. Journal of materials in civil engineering, American Society of Civil Engineers, v. 19, n. 10, p. 848–854.

HUSSEIN, Luaay; AMLEH, Lamya. (2018). Size effect of ultra high-performance fiber reinforced concrete composite beams in shear. Structural Concrete, v. 19, n. 1, p. 141-151.

J Lubliner, J Oliver, S Oller, E Onate. (1989). A plastic-damage model for concrete. International Journal of solids and structures, v. 25, n. 3, p. 299-326.

KMIECIK, P.; KAMIŃSKI, M. (2011). Modelling of reinforced concrete structures and composite structures with concrete strength degradation taken into consideration. Archives of civil and mechanical engineering, v. 11, n. 3, p. 623-636.

KRAHL, Pablo Augusto; CARRAZEDO, Ricardo; EL DEBS, Mounir Khalil. (2018). Mechanical damage evolution in UHPFRC: experimental and numerical investigation. Engineering Structures, v. 170, p. 63-77.

KRUSZEWSKI, Dominic; ZAGHI, Arash E.; WILLE, Kay. (2019). Finite element study of headed shear studs embedded in ultra-high-performance concrete. Engineering Structures, v. 188, p. 538-552.

KUPFER, Helmut; HILSDORF, Hubert K.; RUSCH, Hubert. (1969). Behavior of concrete under biaxial stresses. In: Journal proceedings. p. 656-666.

Labibzadeh, M. (2020). Size effects on concrete damaged plasticity model. Current Trends in Civil &Amp; Structural Engineering, 6(3). doi.org/10.33552/ctcse.2020.06.000637

LEE, Jeeho; FENVES, Gregory L. (1998). Plastic-damage model for cyclic loading of concrete structures. Journal of engineering mechanics, v. 124, n. 8, p. 892-900.

LEUTBECHER, T.; FEHLING, E. (2013). A simple design approach for uhpfrc in bending. n. 1, p. 509–518.

M. Singh, A.H. Sheikh, M.S. Mohamed Ali, P. Visintin, M.C. Griffith (2017). Experimental and numerical study of the flexural behavior of ultra-high performance fiber reinforced concrete beams. Construction and Building Materials, v. 138, p. 12-25.

MA Al-Osta, MN Isa, MH Baluch, MK Rahman. (2017). Flexural behavior of reinforced concrete beams strengthened with ultra-high performance fiber reinforced concrete. Construction and Building Materials, v. 134, p. 279-296.

MAHMUD, Goran H.; YANG, Zhenjun; HASSAN, Aram MT. (2013). Experimental and numerical studies of size effects of Ultra-High-Performance Steel Fibre Reinforced Concrete (UHPFRC) beams. Construction and Building Materials, v. 48, p. 1027-1034.

MANSUR, M. A.; CHIN, M. S.; WEE, T. H. (1999). Stress-strain relationship of high-strength fiber concrete in compression. Journal of materials in civil engineering, v. 11, n. 1, p. 21-29.

MICHAL, S.; ANDRZEJ, W. (2015.) Calibration of the CDP model parameters in Abaqus. In: The 2015 World Congress on Advanced in Structural Engineering and Mechanics. [S.l.: s.n.].

NASRIN, Sabreena; IBRAHIM, Ahmed. (2018). Finite-element modeling of UHPC hybrid bridge deck connections. International Journal of Advanced Structural Engineering, v. 10, n. 3, p. 199-210.

Richard P, Cheyrezy M. (1995). Composition of reactive powder concretes. Cement Concrete Research. 25(7):1501–11.

S Bahij, SK Adekunle, M Al-Osta, S Ahmad, SU Al-Dulaijan, MK Rahman. (2018). Numerical investigation of the shear behavior of reinforced ultra high performance concrete beams. Structural Concrete, v. 19, n. 1, p. 305-317.

S Chen, R Zhang, LJ Jia, JY Wang. (2018). Flexural behavior of rebar-reinforced ultra-high-performance concrete beams. Magazine of Concrete Research, v. 70, n. 19, p. 997-1015.

Schmidt M. (2008). Sachstandsbericht Ultrahochfester Beton Deutscher Ausschuss fur Stahlbeton (DAfStb) vol 561 (Berlin: Beuth Verlag).

SHAFIEIFAR, Mohamadreza; FARZAD, Mahsa; AZIZINAMINI, Atorod. (2018). A comparison of existing analytical methods to predict the flexural capacity of Ultra-High-Performance Concrete (UHPC) beams. Construction and Building Materials, v. 172, p. 10-18.

SLOBBE A.T., HENDRIKS M.A.N., ROTS J.G. (2012). Sequentially linear analysis of shear critical reinforced concrete beams without shear reinforcement, Finite Elements in Analysis and Design, Volume 50, Pages 108-124.

SPECK, Kerstin. (2008). Beton unter mehraxialer Beanspruchung: ein Materialgesetz fur Hochleistungsbetone unter Kurzzeitbelastung. Inst. fur Massivbau, Techn. Univ.

WILLE, K.; EL-TAWIL, S.; NAAMAN, A.E. (2014). Cement & Concrete Composites Properties of strain hardening ultra-high-performance fiber reinforced concrete (UHP-FRC) under direct tensile loading. Cement and Concrete Composites, V. 48, p. 53-66.

YIN, Hor; SHIRAI, Kazutaka; TEO, Wee. (2019). Finite element modelling to predict the flexural behaviour of ultra-high-performance concrete members. Engineering Structures, v. 183, p. 741-755.

YOO, Doo-Yeol; YOON, Young-Soo. (2015). Structural performance of ultra-high-performance concrete beams with different steel fibers. Engineering Structures, v. 102, p. 409-423.